PHYSICAL REVIEW B VOLUME 41, NUMBER 4 1 FEBRUARY 1990

Computer simulations on collision-cascade anisotropies: Bombardment of single-crystalline Cu(100) by Ar ions

M. Hautala
Department of Physics, University of Helsinki, Siltavuorenpenger 20 D, SF-00170 Helsinki, Finland

J. Likonen
Technical Research Centre of Finland, Reactor Laboratory, Otakaari 3 A, SF-02150 Espoo, Finland

(Received 10 May 1989)

The distributions of the recoil vector fluxes are studied using the binary collision lattice simulation code COSIPO in order to investigate the development of collision-cascade anisotropies in single-crystalline Cu. The vector fluxes are directly related to the angular distributions of sputtered particles. A single-crystal Cu(100) surface is used as the target, and is bombarded with normally incident 5-keV Ar ions. The results are discussed within the framework of focusing. The collision cascades are dominated by focusing along the ⟨110⟩ directions. Anisotropies in collision cascades turned out to be dependent on the interaction potential. The anisotropy in simulated angular distributions of sputtered particles is directly related to anisotropies in collision cascades.

I. INTRODUCTION

Ion bombardment of metal surfaces gives rise to atomic collision cascades, which result in several processes such as damage production, sputtering, and mixing. Cascades are usually described by the linear-cascade model,[1,2] where it is assumed that the cascade is dilute, i.e., that there are no collisions between moving atoms, and that the target is amorphous. In general, linear-cascade models use the approximation that the flux of low-energy recoils is isotropically distributed.[2] These linear-cascade theories can be extended to cover anisotropy effects.[3-5] In these approaches, the anisotropy of the recoil flux is directly related to the momentum of the incoming ions. Other techniques based on transport equations have also been developed.[6,7] Analytical treatments generally involve more or less severe approximations, such as ignoring the crystal structure of the target and inelastic energy losses or restricting the treatment to hard-core or other simplified atomic scattering laws. In crystalline targets the regular arrangement of atoms cannot be neglected, because correlated collision sequences propagate effectively along or parallel to atomic rows and planes. The basic features of linear correlated recoiling sequences were suggested first by Silsbee,[8] while Nelson[9] extended the focusing sequence mechanism to the case of thermally vibrating atomic rows. From the experimental viewpoint the collision cascades are experimentally accessible through studies of the angular[10-12] and energy[13,14] distributions of the sputtered particles.

Computer simulation is a very powerful method for studying atomic collision processes in solids because many of these approximations can be omitted. A number of computer simulation sputtering experiments have in fact been performed (for reviews see Refs. 15–18) but rather little attention has been given to studies of the collision cascades themselves. In the early days of molecular dynamics calculations specific features of individual cascades were investigated in connection with radiation damage.[19-21] We have previously studied collision cascade anisotropies both in amorphous and crystalline targets.[22,23] Hou has studied individual cascades by component analysis[24] and by using the theory of fuzzy sets[25] together with the binary collision computer simulation code MARLOWE.[26] Recently Hou and Eckstein have calculated the distributions of particle momentum directions in collision cascades.[27] They investigated the evolution of the collision cascade anisotropies as a function of the recoil energy and the relation of anisotropies to sputtering from Au(111) surfaces.

The initial aim of the present paper was to answer two questions that are partly connected with each other. In previous calculations we found that recoil vector-flux distributions were peaked at polar angle $\theta = 90°$ for 40-keV Ne normally incident on a (100) surface Al single crystal.[23] It was hoped that the present distributions, which are not averaged about the azimuthal angle, would enlighten us concerning the physical reason for these peaks. On the other hand, we have recently studied the sputtering of Cu of different structures by 5-keV Ar ions in some detail.[28] In the monocrystalline case the ⟨101⟩ Wehner spots[29] could be observed. The present calculations are intended to give more detailed information about the origin of these peaks, i.e., on the development of the collision cascade anisotropies and on the mechanisms that cause focusing during the collision cascades. The evolution of the collision cascade is studied as a function of the distance from the surface and the strength of the interaction potential. In recent computer simulations it has been observed that the angular distributions of sputtered particles are strongly dependent on the interaction potential.[30,31] The Molière potential with Robinson's screening lengths gave better agreement with experimental data than the so-called universal potential in the case of 600-eV Xe in Au(111).[30] Thus, it is quite natural to expect that the changes observed in the angular distributions of sputtered particles are at least partly connected to different focusing properties of various interaction potentials.

It will be shown that the angular distributions of the sputtered particles and the recoil vector-fluxes may be directly compared with each other. This enables the study of the development of the angular distributions of backward and forward sputtered particles as a function of the position of a hypothetical surface. In this paper we concentrate on presenting the method of the calculations and the various concepts and distributions which are accessible through the method. The contribution of various collision sequences and low-energy channeling to modified recoil vector flux and sputtering as a function of recoil energy will be treated more thoroughly in a subsequent paper.[32]

II. METHOD OF CALCULATION

A. The assumptions

In the studies of anisotropies we have used the COSIPO code,[33] with the following assumptions in the calculations.

(1) Only collisions with impact parameters less than $p_{\max}$ are considered. $p_{\max}$ is chosen to be half of the lattice constant $a = 3.6$ Å. The next main scatterer is the nearest one (distance x_i) that has the impact parameter b_i less than $p_{\max}$. The subsequent collisions are treated as simultaneous with the main collision: if the impact parameter b_j is less than $p_{\max}$ and the distance x_j is less than $x_i + \Delta x$. A value of 0.4 Å is used for Δx. The energy losses of these collisions are taken into account. The deflections of the nearly simultaneous collisions are included only if b_j is less than $1.5b_i$. Each of the simultaneous collisions is carried out as if it were occurring alone. The several deflections of the projectile due to each collision are added vectorially. For more details and for the consequences of the assumptions and parameters on sputtering see Ref. 31.

(2) The surface is represented by a planar barrier with a surface binding energy E_s=4 eV.[28] To account for realistic lengths of collision sequences an amount of $E_b = 0.2$ eV is subtracted from the kinetic energy of every atom leaving its lattice site.[18] This value for the model parameter is an appropriate choice for the $\langle 110\rangle$ chains; for the $\langle 100\rangle$ and $\langle 111\rangle$ chains it may be an underestimation.[18]

(3) Lindhard-Scharff-Schiøtt[34] (LSS) velocity-proportional electronic stopping is assumed. In the present paper electronic energy loss during collisions is ignored.

(4) The collision cascades are sufficiently dilute that the target atoms can be assumed to be at rest prior to a collision with a primary or secondary particle. A target atom is considered to be displaced when recoiling with kinetic energy larger than a threshold value E_d. A value of 4 eV is used for E_d in all cases. The recoils in the cascades are followed until their energy falls below a threshold energy $E_c = 4$ eV. The threshold value $E_c = 4$ eV is chosen as the low-energy cutoff since in sputtering simulations E_c is usually taken close to the surface binding energy E_s. This is due to the fact that recoils having energy less than E_s cannot be sputtered.

(5) The interaction potential $V(r)$ is assumed to be a screened Coulomb potential with Thomas-Fermi screening length; the screening function is either the Molière function or it is a mean potential obtained by fitting a sum of exponentials to 50 ion-atom potentials obtained using Dirac-Fock calculations of the electron densities.[35] The mean potential is close to the so-called universal potential.[36,37] The effect of the neighbouring atoms on the scattering potential is estimated with the potential[38]

$$U(r) = \begin{cases} V(r) + V(2r_c - r) - 2V(r_c), & r < r_c \\ 0, & r \geq r_c \end{cases} \qquad (1)$$

$V(r)$ is the mean potential. The effect of the form of (1) is mainly that the zero of potential occurs at $r = r_c$. Here r_c is chosen to be half of the lattice constant. The potentials used in the simulations are shown in Fig. 1 for Cu-Cu interactions.

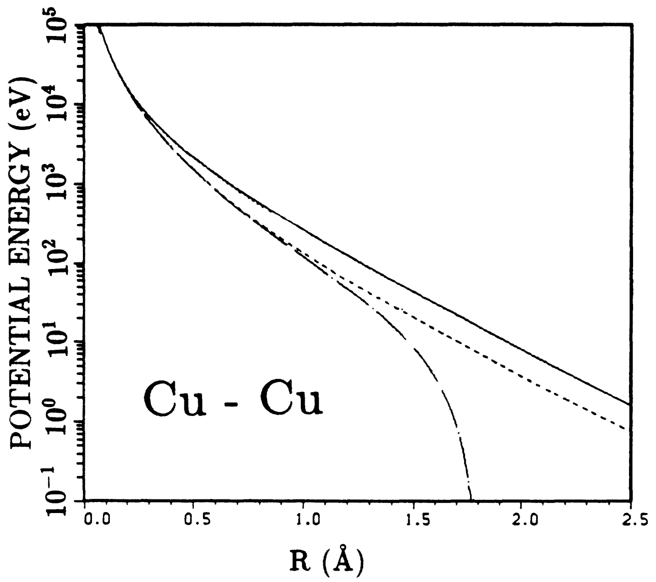

FIG. 1. Comparison of different potentials for Cu-Cu interaction used in the simulations. Molière (——), mean (- - - - - -), and eroded mean (— · —). Thomas-Fermi screening length is used in all potentials.

(6) Elastic scattering described by classical dynamics is assumed.

(7) The effects of mass transport by the recoil fluxes[39] are assumed to be negligible and thus the density is constant. The cascades take place in a perfect crystal.

(8) Energy transport due to electronic cascade effects is neglected.

(9) The projectiles are 5-keV Ar ions.

(10) Thermal displacements are included by assuming that they are uncorrelated and Gaussian distributed. The target temperature is 300 K in the simulations. The root-mean-square displacement (0.08 Å) of the target atoms is based on the Debye model.

Assumption number (7) is most severe. The assumption of the crystal remaining perfect is not completely fulfilled. In the case of sputtering the yield is slightly higher without the erosion of the surface than with it.[31] When studying the evolution of the cascade anisotropies the assumption should not be so bad since, as will be seen, the ⟨110⟩ collision sequences are dominating and in fact, very little mass transport takes place. Furthermore, we are working in the linear-cascade regime and thus the cascade is dilute. From the theoretical point of view it is interesting to see how the cascade will develop in an ideal crystal.

Assumption number (1) may also be questioned and, as already thoroughly discussed by Robinson and Torrens,[26] the Cu-Cu collisions may be regarded as strictly binary only above the order of 10 eV. The trajectories between the collisions are approximated by straight lines and the ions and recoils always move along the *asymptotes*. The binary collision assumption fails when the next collision occurs before the trajectory practically reaches the asymptote. This fact is taken into account by the special treatment of nearly simultaneously occurring collisions and as shown in Ref. 31 the results are insensitive to the parameters that regulate the treatment of these collisions. In addition, we emphasize the fact that we are only discussing qualitative aspects and that quantitative numbers are omitted.

The calculation of asymptotes instead of real trajectories has an essential benefit. It would be very difficult to determine the direction of a recoil in a case of real trajectories since the trajectories are invariably curved. In determining the flux distributions the direction of recoils must be known. In other words, the present kind of calculation would not be straightforward for molecular dynamics simulations.

B. The geometry and the distributions

Figure 2 illustrates the geometries employed in the simulations. The 5-keV Ar projectile ions are incident along the z direction and impinge on the target surface at normal incidence. $\theta = 0°$ corresponds to the inward surface normal and $\theta = 180°$ to the outward normal. The resulting cascades from 5000 projectile ions are followed and when a recoil passes through a marker, its direction and momentum vectors are logged. The projectiles hit the surface at a random position. The marker planes have no thickness and they are parallel to the surface. The locations of the marker planes are indicated in the figure captions. From the resulting angular distributions of recoils and recoil momentum crossing marker planes the recoil vector flux $N_r(\theta,\phi)$ and the momentum vector flux $N_p(\theta,\phi)$ are calculated. These fluxes represent the directional derivative of the recoil flux and momentum flux, respectively, for recoils with energy greater than the threshold value E_c.[40] In the present paper momentum distributions will not be studied. It should be realized that in the calculations the flux distributions correspond to 5000 incoming ions and they are presented in arbitrary units. In a real experiment the flux of recoils is proportional to the flux of incoming ions, which generates a stationary distribution of moving target atoms. The vector-flux distributions do not depend on the lateral directions x and y. The distributions will be presented as stereographic projections. Figure 3 shows the stereographic projection for the (100) surface. Only those directions are presented which are observed in the simulations.

It turns out that the calculations may be used to reveal different features from the cascades depending on which criterion is used when a particle crosses a marker. This is due to the treatment of a collision. As already explained, the trajectories between the collisions are approximated by straight line-segments, and the ions and recoils always move along their *asymptotical* trajectories.

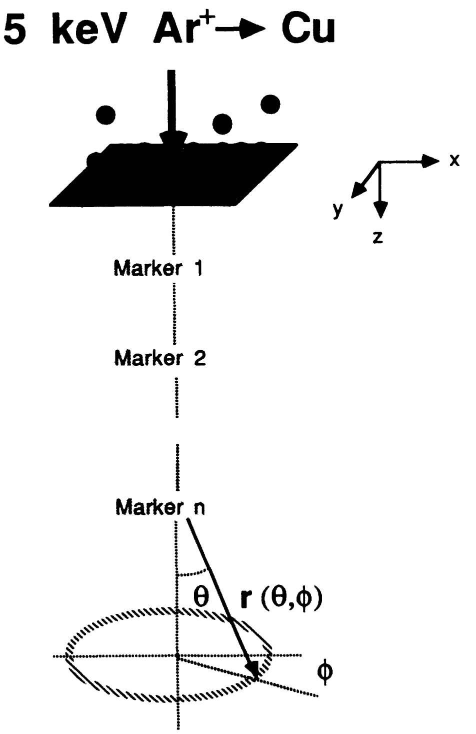

FIG. 2. Schematic illustration of the geometry used in the simulations.

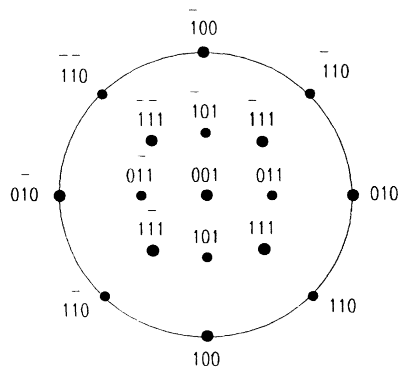

FIG. 3. Stereographic (100) projection for a fcc crystal.

This results in corrections to the initial position of the asymptotes which also require calculation of the so-called time integral.[26] These corrections mean that the point of deflection of the trajectory of the projectile is shifted back in the laboratory system by an amount x_1 and the initial position of the recoil is moved in the forward direction along the incoming asymptote by an amount x_2. The classical scattering theory and the solution of the equations of motion are thoroughly treated in Refs. 26 and 41.

In the present calculations the correction x_2 in the trajectory of the target atom is always less than 0.5 Å but the correction x_1 in the trajectory of the projectile becomes significant at low energies in particular. We have previously pointed out that sputtering data are not sensitive in setting an upper limit for x_1 or x_2.[31] In the head-on collision of Cu-Cu the backup x_1 is of the order of the distance between the (110) crystal planes when the energy is about 10 eV. We take advantage of this property of backup of asymptotical trajectories by producing in each simulation two kinds of data.

(1) In the first case the backup of the projectile was omitted when it was checked whether the recoil has passed a marker or not. After this check the backup is taken into account in the trajectory of the projectile. This is just a technical procedure in order to ascertain that momentum flux is continuous and is correctly calculated. Note that the asymptotical trajectories are calculated correctly. Now all the chains are seen in the distributions. The momentum vector flux N_p describes correctly the transmission of momentum. The recoil vector-flux N_r calculated in this way does not properly give the mass flow since some low-energy recoils that in fact do not cross the marker due to the backup are also included. We call this flux the modified recoil vector flux N_r^m. In the sputtering process the transport of matter inside the crystal and thus the recoil vector flux N_r are not relevant quantities. However, the N_r^m distribution (inside the target) may be compared directly with the distribution of sputtered particles and is therefore a very valuable quantity.

(2) In the second case the corrections in the trajectories were taken into account before the check of the eventual marker crossing was performed. In this instance the low-energy $\langle 110\rangle$ chains are not observed in all cases. The resulting recoil vector fluxes N_r show the *mass* flow in the cascade. The differences between the N_r and N_r^m distributions are directly related to energy transfer without mass. If the marker were above the surface, N_r and N_r^m distributions would be identical.

The distribution of sputtered particles can be directly calculated from the modified recoil vector flux N_r^m in the following way. The current of particles through a marker at depth z in direction $(\theta, \theta+\Delta\theta; \phi, \phi+\Delta\phi)$ is

$$J(z) = C \int_{\theta}^{\theta+\Delta\theta} \int_{\phi}^{\phi+\Delta\phi} N_r^m(\theta,\phi,z) \sin\theta \, \cos\theta \, d\theta d\phi \; . \tag{2}$$

C is a constant including the current of incoming ions. For the bin width we used 5°. The angular distribution of sputtered particles $N_s(\theta,\phi)$ may similarly be obtained from

$$J(0) = C \int_{\theta}^{\theta+\Delta\theta} \int_{\phi}^{\phi+\Delta\phi} N_s(\theta,\phi) \sin\theta \, d\theta d\phi \; . \tag{3}$$

Thus $N_s(\theta,\phi) = N_r^m(\theta,\phi,z=0)\cos\theta$. Here N_s does not yet include the surface barrier test. Thus *we may study the development of $N_s(\theta,\phi)$ as a function of the hypothetical surface position by changing z in $N_r^m(\theta,\phi,z)$*. The equation (2) shows that the statistics of N_r^m in the calculations are proportional to $1/\{\cos(2\theta) - \cos[2(\theta+\Delta\theta)]\}$. Therefore the statistics of N_r^m (as well as of N_r) at angles corresponding to the beam direction and to the surface are poorer by up to a factor of 10 compared to other angles in the case of isotropic flux, i.e., when N_r^m is a constant.

In previous papers,[22,23] in which mainly structureless targets were under study, N_r and N_p were averaged about the azimuthal angle ϕ and as a consequence the features associated with crystal symmetry perpendicular to the ion beam disappeared. Our method of studying fluxes differs from the calculations of the energy resolved distributions of particle momentum directions by Hou and Eckstein,[27] who have no depth resolution, except at the surface where they use a slab with a thickness of about one atomic spacing around the surface plane. The energy resolution will be studied in a subsequent paper.[32]

III. RESULTS AND DISCUSSION

A. The role of marker position with respect to atomic planes

In this section we shall study the recoil vector flux distributions as a function of the depth of the marker in order to show the strong influence of the backup of low-energy recoils. If the marker position coincides with a crystal plane, the distributions are dominated by recoils moving in the $\langle 100\rangle$ and $\langle 110\rangle$ directions along the crystal

tal plane. On the other hand, when the marker is in the middle of two (100) atomic planes (as is usually the case in the following) those recoils moving along the crystal planes, which are parallel to the surface, do not pass through the marker. However, recoils with momentum directed parallel to the surface also have an influence on the cascades as well as on the flux distributions because after one or several collisions the momentum is usually directed either downward or upward. These recoils are then observed in the flux distributions. Thus when the N_r^m distributions are studied the marker may (or rather, must) be in the middle of two crystal planes without losing essential information. Equations (2) and (3) may be compared as discussed.

In fact, the position of the marker planes plays an important role in the case of the recoil vector flux N_r, which describes the mass flow in the cascades. This is because low-energy recoils do not cross a marker plane if the backup is larger than the distance between the marker and the site of the recoil as measured in the direction of the projectile. Another fact which complicates the situation is inherent in the crystal structure itself. Take for example the ⟨100⟩ chains and the fcc (100) surface. Half of the ⟨100⟩ rows intersecting the (100) surface have the last atom at the surface and the other half at depth $z = 1.8$ Å. This means that if the marker plane is somewhere between the first and second (100) atomic plane, all those chains having their last atom at the second atomic plane cross the marker irrespective of the backup. On the other hand, the other type of ⟨100⟩ chains cross the marker depending on the position of the marker and the backup. For the momentum flux N_p and modified recoil flux N_r^m this is not relevant, because the contribution to the flux is calculated before the backup. Notice that we calculate only the kinetics, but do not check whether a replacement collision occurs or not.

In Fig. 4 we have chosen one plane interval 3.6–5.4 Å for a detailed study. A Cu (100) surface is bombarded at normal incidence with 5-keV Ar ions. The marker is situated at depths 3.8, 4.2, 4.6, and 5.0 Å, and the Molière potential with Thomas-Fermi screening lengths for Ar-Cu and Cu-Cu interactions and $E_c = 4$ eV are used. The recoil flux distributions N_r are shown both in the forward and backward direction. Some of the distributions are rather isotropic and the statistical inaccuracy discussed earlier is evident. The peaks near the edges have to be considered separately. The differences between the recoils going up or down in the mass flows are pronounced at first. This is due to the fact that the cascade is not yet well developed. On the other hand, the backup of recoils has an appreciable effect on the distributions. When the marker is at depth $z = 3.8$ Å the recoil flux distribution in the forward direction [Fig. 4(a)] shows four $\theta = 90°$ peaks, which coincide with the ⟨110⟩ directions in the (100) planes. In addition to these peaks, there are four smaller ⟨100⟩ peaks ($\theta = 90°$) in Fig. 4(a). In the backward direction the recoil flux distribution [(Fig. 4(b)] is more or less structureless except for the ⟨110⟩ and ⟨100⟩ peaks at $\theta = 90°$. Calculations show that the $\theta = 90°$ peaks are slightly asymmetric, the maxima being at θ just less than 90°. This is due to the fact that the recoils moving approximately along the (100) plane may cross the marker which is 0.2 Å below the atomic plane only if θ is slightly less than 90°. This asymmetry could also be a consequence of the fact that ions are channeled in the [001] direction and scattering kinematics limit primary recoils to the angular range $0° < \theta < 90°$.[23]

At depth $z = 4.2$ Å the recoil flux distribution is practically structureless in the backward direction [Fig. 4(d)]. The ⟨110⟩ peaks are missing due to the backup of re-

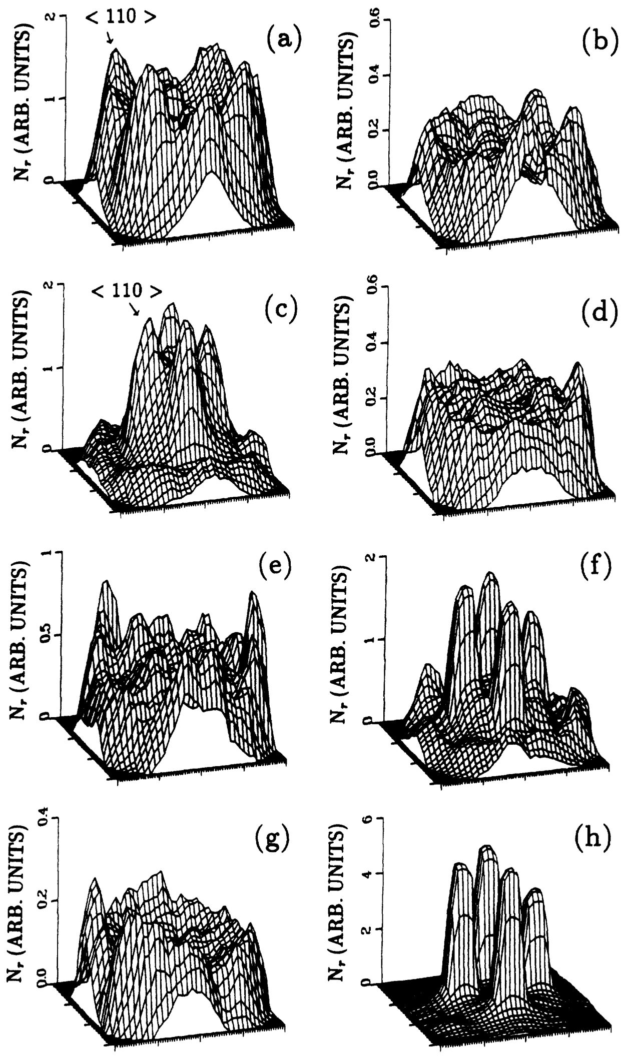

FIG. 4. The stereographic projection of the recoil vector-flux distributions $N_r(\theta, \phi, z)$ at depths 3.8 Å, (a)–(b); 4.2 Å (c)–(d); 4.6 Å (e)–(f); and 5.0 Å (g)–(h) for 5-keV Ar normally incident on a (100) surface Cu single-crystal. The Molière potential is used. The distributions of the forward directed recoils are presented on the left-hand side while the right-hand side shows the distributions of backward directed recoils.

coils as discussed earlier. In the forward direction [Fig. 4(c)] the recoil flux distribution is dominated by four $\theta = 45°$ peaks, which correspond to the ⟨110⟩ directions intersecting the marker. These peaks are not observed in Fig. 4(a), because the cascade is not yet fully developed and because the marker is situated so near the (100) atomic plane that the distribution was dominated by recoils moving nearly parallel to this atomic plane. The $\theta = 90°$ peaks are missing because the marker plane is 0.6 Å from the nearest (100) plane and the recoils moving along this (100) plane are not able to cross the marker.

At depth $z = 4.6$ Å the recoil flux distribution in the forward direction is almost structureless except $\theta = 90°$ peaks [Fig. 4(e)]. There are, however, very small ⟨111⟩ ($\theta = 55°$) and ⟨100⟩ ($\theta = 0°$) peaks in the distribution. The absence of the ⟨110⟩ peaks is due to the fact that the marker is quite near to the atomic plane at depth $z = 5.4$ Å and thus the recoils do not cross the marker because of the backup. The distribution in the backward direction [Fig. 4(f)] shows four pronounced ⟨110⟩ peaks. When the marker is at depth $z = 5.0$ Å the distributions are quite similar to the corresponding distributions at depth $z = 4.6$ Å. However, the ⟨110⟩ peaks in Fig. 4(h) are more dominant than in Fig. 4(f). This again results from the backup of recoils, because many of the recoils crossing the marker at depth $z = 5.0$ Å do not necessarily pass through the marker at depth $z = 4.6$ Å. The recoils moving in the ⟨110⟩ direction are more energetic in Fig. 4(f) than in Fig. 4(h) because in Fig. 4(f) the marker is farther away from the (100) atomic plane at depth $z = 5.4$ Å than in Fig. 4(h) and thus the recoils must have smaller backup in order to pass the marker.

B. The collision chains

Before going into details of the depth dependence of the distributions we give here a short summary of the mechanisms that are responsible for the momentum flow in the fcc crystal. This topic has been extensively discussed in Ref. 18.

The regular arrangement of atoms in a crystal lattice has an important influence on the character of collision cascades. In the face-centered cubic crystals collision chains occur mainly in the ⟨110⟩, ⟨100⟩, and ⟨111⟩ directions. In the case of the ⟨100⟩ and ⟨111⟩ rows, which are not closely packed, assisted focusing[18] is especially important, but it also delivers a significant contribution for the closely packed ⟨110⟩ rows. In the case of the ⟨100⟩ row the focusing ring is formed by a square of the four nearest neighboring atoms with distances being 1.8 Å from the ⟨100⟩ row. For the ⟨111⟩ row the situation is even more complicated because there are two focusing rings formed by six atoms instead of one ring and the distances of the ring atoms from the ⟨111⟩ row are 1.47 Å. This implies that energy losses to the focusing rings are larger for the ⟨111⟩ row than for the ⟨100⟩ row. For the ⟨110⟩ row the energy losses are even less than for ⟨100⟩. It is clear from the considerations of geometries of the focusing rings that the focusing energy[8] is highest for the ⟨111⟩ row and lowest for the ⟨110⟩ row. Robinson[18] and Shulga[42] have calculated focusing energies for different potentials and rows based on dynamical calculations. These values for Cu (Ref. 18) are in the case of the Molière potential with Robinson's screening lengths: 17 eV (⟨110⟩), 20 eV (⟨100⟩), and 225 eV (⟨111⟩). One must remember that these values for the focusing energy are estimates and can only give the correct order of magnitude, because the focusing energy varies from collision to collision and it also depends upon the collision kinematics. Collision sequences along non-close-packed rows fcc ⟨100⟩ and ⟨111⟩ apparently always involve replacements.[18] In closely packed rows fcc ⟨110⟩ defocusing chains seem to involve replacements but focusing collisions need not do so. According to the sputtering calculations by Hou[43] the contribution of replacements is over 40% in the case of ⟨110⟩ spots in sputtering of Cu(100) by 5-keV Ar ions. Yamamura[44] has pointed out in his computer simulations that the contribution of focusing and assisted focusing to sputtering yields varies from 36% to 69% depending on the crystal orientation when single-crystalline Cu was bombarded with 1-keV Ar ions and thermal uncorrelated vibrations were included. The present calculations are not concerned with whether or not the projectile replaces the next row atom on its lattice site.

C. The depth dependence of the collision cascade

In the following we will study the evolution of the anisotropies of a *statistical* cascade as a function of the depth of the marker using the N_r^m distributions, which bears a resemblance to the distribution of sputtered particles. The effect of the interatomic potential on the N_r^m distributions will also be investigated. It should be stressed that individual cascades may drastically deviate from the statistical behavior depending on the impact position of an ion.

Figures 5–7 present the development of a statistical cascade as a function of distance from the surface and interaction potential. A Cu(100) surface is irradiated at normal incidence with 5-keV Ar ions. The marker planes are situated symmetrically in the middle of two crystal planes. The Molière potential is used in Fig. 5. Figure 5(a) displays the modified recoil flux distribution N_r^m in the backward direction when the marker is at depth $z = 2.7$ Å. The distribution is dominated by four $\theta = 45°$ peaks, which correspond to focusing along the ⟨110⟩ directions. Calculations reveal that the modified recoil flux distributions in the backward direction are dominated by these ⟨110⟩ peaks in all symmetrical positions of the marker planes. Figure 5(a) was chosen just as an example. Figures 5(b)–5(h) present the modified recoil flux distributions in the forward direction when the marker is at depths z = 2.7, 4.5, 6.3, 8.1, 9.9, 11.7, and 13.5 Å, respectively. Nearer the surface the modified recoil flux distributions in the forward direction are more or less structureless, which means that the cascade is undeveloped. The distribution in the forward direction at depth $z = 2.7$ Å [Fig. 5(b)] shows four very small $\langle 111 \rangle$ peaks ($\theta = 55°$), which, however, have disappeared in Fig. 5(c). Figures 5(b)–5(h) reveal that the $\langle 110 \rangle$ peaks start to develop also in the forward direction at the depth $z \approx 4.5$ Å and that they become more distinct when the depth of the marker plane increases. Further calculations show that the modified recoil flux distributions in both directions are dominated by focusing along the $\langle 110 \rangle$ directions at least up to the projected range $R_p \approx 60$ Å of the incoming ions.

The distributions of the impact parameter of the recoils were also calculated, and they showed a pronounced maximum corresponding to the $\langle 110 \rangle$ peaks and head-on collisions in the case of Fig. 5(a). Head-on collisions mean in this situation that the direction of the recoil is the same as the direction of the colliding particle prior to the collision. The impact parameter may be of the order of 0.1 Å at low energies for this circumstance to be fulfilled. Although the distributions of impact parameter have a pronounced maximum corresponding to focusing chains, other types of collision chains also have an important role in focusing along the $\langle 110 \rangle$ directions. These distributions show that the focusing sequences represent about half the contribution to the $\langle 110 \rangle$ peaks and that they are dominated by head-on collisions at all symmetrical marker positions. In the forward direction the impact parameter distributions show very clearly the development of the cascade as a function of depth. The significance of the focusing chains in the $\langle 110 \rangle$ peaks ($\theta = 45°$) grows as the depth of the marker increases but

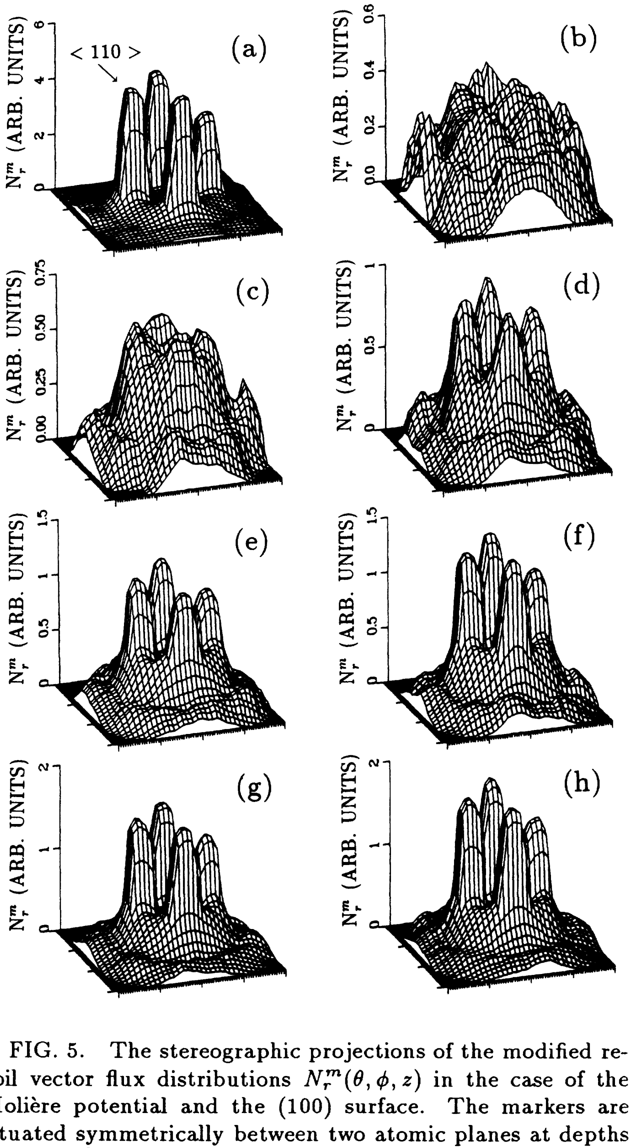

FIG. 5. The stereographic projections of the modified recoil vector flux distributions $N_r^m(\theta, \phi, z)$ in the case of the Molière potential and the (100) surface. The markers are situated symmetrically between two atomic planes at depths $z = 2.7$ Å (a)–(b); 4.5 Å (c); 6.3 Å (d); 8.1 Å (e); 9.9 Å (f); 11.7 Å (g); and 13.5 Å (h). The distribution is for backward directed recoils in (a) and for forward directed recoils in (b)–(h).

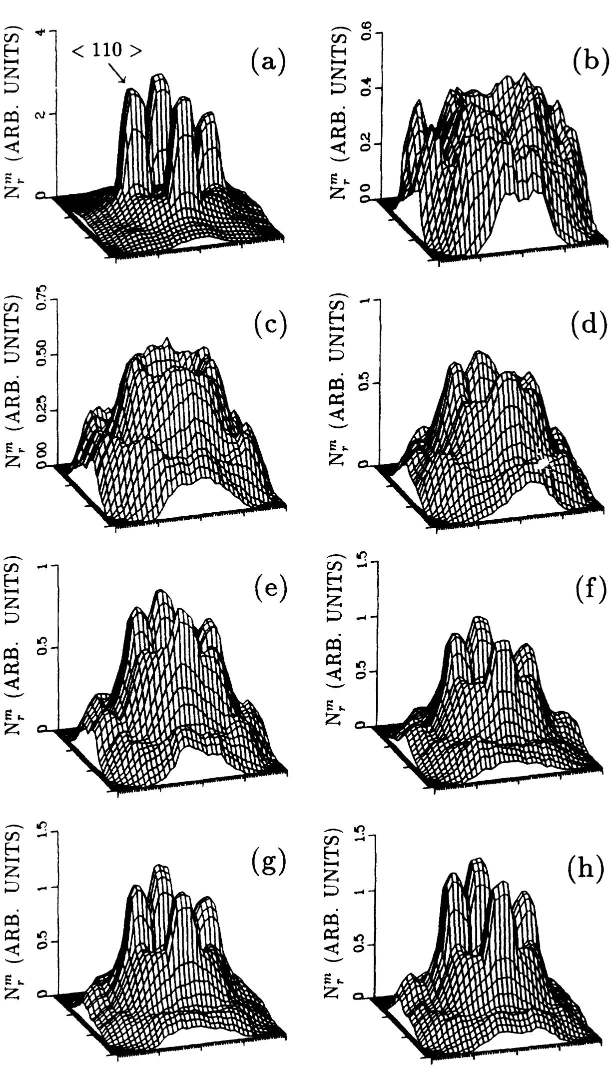

FIG. 6. Stereographic projections of the modified recoil vector flux distributions $N_r^m(\theta, \phi, z)$ as in Fig. 5 but using the mean potential instead.

the other mechanisms (e.g., defocused and replacement chains, low-energy channeling) have a major contribution. The relative contribution of the focusing sequences to the ⟨110⟩ peaks is about 20% in Fig. 5(d) and 40% in Fig. 5(h).

The difference between the mass and momentum fluxes can be noticed when the recoil flux in Fig. 4(e) and the modified recoil flux in Fig. 5(c) are compared with each other. The distribution in Fig. 4(e) is almost structureless whereas in Fig. 5(c) there are four small ⟨110⟩ peaks. This difference becomes more evident deeper in the target and when the marker is situated symmetrically in the middle of two atomic planes. The mass flow is practically structureless in the forward direction and the ⟨110⟩ peaks are just discernible in the backward direction, but the modified recoil flux is dominated by the ⟨110⟩ peaks in both directions.

Figure 6 shows the modified recoil flux at the same marker positions as in Fig. 5, but now the mean potential is used. In the backward direction the modified recoil flux distribution is dominated by focusing along the ⟨110⟩ directions at all symmetrical marker positions [see Fig. 6(a)] in the same way as with the Molière potential. The development of the cascade in the forward direction as a function of depth [see Figs. 6(b)–6(h)] is analogous to the Molière potential case. In the forward direction the ⟨110⟩ peaks start to develop at the depth $z \approx 6.3$ Å and they become more pronounced deeper in the target. Thus, the ⟨110⟩ peaks emerge somewhat deeper in the target than in Fig. 5. This is due to the poorer focusing efficiency of the mean potential compared to that of the Molière potential.[18,42] The modified recoil flux distributions are also dominated by the ⟨110⟩ peaks in both directions, when the position of the marker is of the order of the projected range of the incoming ions ($R_p \approx 90$ Å). The impact parameter distributions are analogous to the Molière potential case, and they show a pronounced maximum corresponding to the ⟨110⟩ peaks in the backward direction and the head-on collisions. In the forward direction the relative contribution of the focusing chains grows as the depth of the marker increases. The other mechanisms mentioned earlier make, however, a major contribution to the ⟨110⟩ peaks.

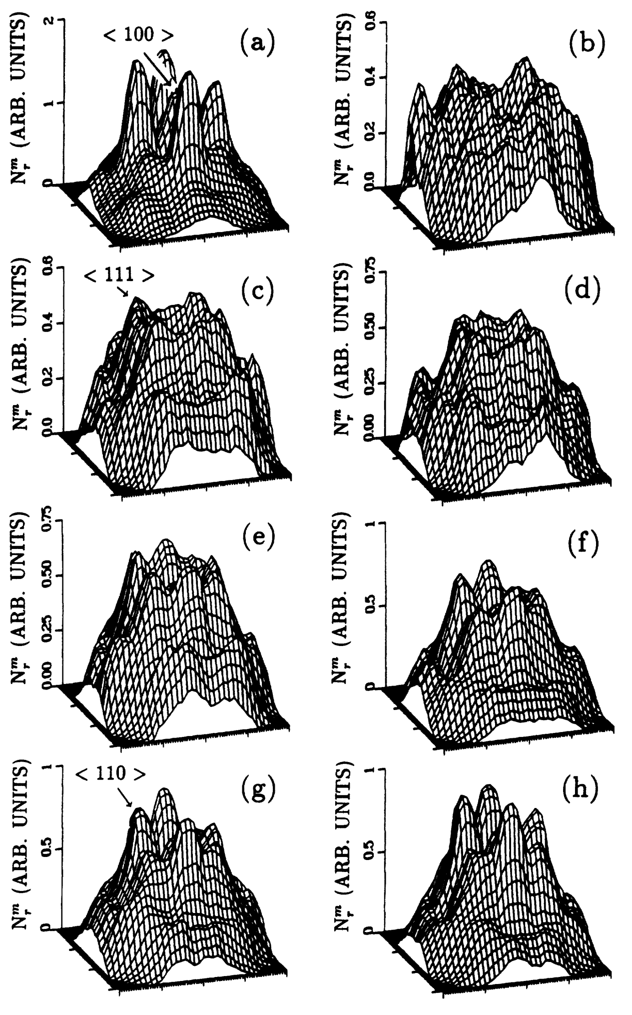

FIG. 7. Stereographic projections of the modified recoil vector-flux distributions $N_r^m(\theta, \phi, z)$ using the eroded mean potential. Otherwise as in Fig. 5.

The effect of the erosion of the interaction potential is studied in Fig. 7, where the mean potential is modified as described in Sec. II. In the backward direction the modified recoil flux distribution is dominated by focusing along the ⟨110⟩ and ⟨100⟩ directions at all symmetrical marker positions [see Fig. 7(a)]. This ⟨100⟩ peak was not observed in Figs. 5 and 6. The development of the cascade in the forward direction differs somewhat from the mean potential case. At depths $z = 2.7$, 4.5, and 6.3 Å [Figs. 7(b)–7(d)] there are four small $\theta = 55°$ peaks that correspond to the ⟨111⟩ directions. Deeper in the target the ⟨110⟩ peaks become more pronounced and the ⟨111⟩ peaks remain more or less unchanged. The ⟨100⟩ peak also emerges deeper in the target but it is not as pronounced as in the backward direction. The impact parameter distributions show a maximum corresponding to the ⟨110⟩ peaks in the backward direction and the head-on collisions. The other mechanisms make, however, a major relative contribution to the ⟨110⟩ peaks. In the case of the ⟨100⟩ peak the collision sequences and low-energy channeling are the principal mechanisms of the modified recoil flux, with the focusing chains making only a minor contribution. In the forward direction the situation is not so straightforward. The impact parameter distribution again shows the development of the cascade as a function of the depth. The focusing sequences contribute more and more to the ⟨110⟩ peaks as the depth of the marker increases. The principal mechanisms in the ⟨100⟩ and ⟨111⟩ peaks are the collision sequences and low-energy channeling while focusing chains make only a minor contribution. The ⟨110⟩ sequences are associated with low-energy recoils and ⟨111⟩ with higher-energy recoils.

Attempts were made to resolve the origin of the ⟨110⟩ chains as well as the reason for the emergence of the ⟨100⟩ peak if the mean potential was eroded. No single reason could be detected by following the collision kinematics. The emergence of the peaks as the cascade develops would tend to indicate that the peaks are simply due to the better transport of momentum along certain directions. Even though a cascade were initially isotropic it would necessarily turn to anisotropic because some directions are more open than others.

IV. COMPARISON WITH SPUTTERING STUDIES

Finally we make a preliminary study on the relation between the angular distribution of the sputtered particles and the cascade anisotropies. A Cu(100) surface is bombarded at normal incidence with 5 keV Ar ions, and the eroded mean potential is used. Figure 8 presents the angular distribution of the sputtered particles for the case of an isotropic surface barrier [Fig. 8(a)] and also a planar barrier [Fig. 8(b)]. The surface binding energy E_s is the same as the threshold energy $E_d = 4$ eV. The distribution of the sputtered particles [Fig. 8(a)] is quite similar to the corresponding marker distribution in Fig. 7(a). The differences between these two figures are due to the surface barrier in Fig. 8 and the fact that the modified recoil flux distributions have to be multiplied by $\cos\theta$ in order to obtain the corresponding distribution of sputtered particles. This relation was discussed in Sec. II. The flux distribution at depth $z = 2.7$ Å in Fig. 7(a) is similar to the corresponding marker distribution at depth $z = 0.9$ Å. It is clear that the simulated angular distribution of the sputtered particles is directly related to the anisotropy of the cascade development. When the refraction of the trajectories is taken into account [Fig. 8(b)], the distribution of the sputtered particles changes markedly, because an ejected atom may be sputtered only if the normal component of its velocity can surmount the planar barrier used in the calculations. The decrease of the ⟨110⟩ ($\theta = 45°$) peak intensity with respect to the central ⟨100⟩ peak in the sputtering distribution is thus rather natural. In addition to this, the refraction of the trajectories also changes the positions of the ⟨110⟩ peaks towards the surface in Fig. 8(b). According to the MARLOWE simulations the contribution of replacement sequences to the ⟨110⟩ spots is over 40%.[43] However, replacement sequences do contribute to ejection in other directions, too. Figure 8(b) shows strikes in directions parallel to the {100} planes intersecting the surface.

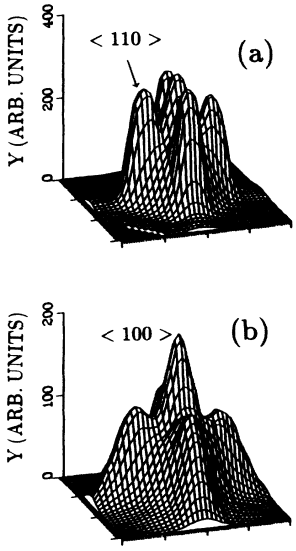

FIG. 8. Stereographic projections of the angular distributions of sputtered particles when the (100) surface is bombarded at normal incidence with 5-keV Ar ions. In (a) the isotropic potential barrier is used, and in (b) the planar barrier. The eroded mean potential is used in both cases.

The experimental distributions of sputtered particles[45] show four ⟨110⟩ spots and one ⟨100⟩ spot. The intensity of the ⟨100⟩ spot is of the same order as the intensity of the ⟨110⟩ spots. Thus, the distribution in Fig. 8(b) is in moderate agreement with experimental results although the combination of the interaction potential and the electronic energy loss used here does not provide the best prediction of sputtering yield and angular distribution.[31] As already explained our model parameters may overestimate the length of the ⟨100⟩ and ⟨111⟩ chains. This would lead to the enhancement of the ⟨100⟩ spot. The main purpose here was to show the relation between the distribution of the sputtered particles and the cascade anisotropies. This connection will be studied further in Ref. 32 with a more reasonable interaction potential and electronic energy loss using energy resolution.

V. CONCLUSIONS

The present paper shows the feasibility of studying the overall anisotropies of the collision cascade using the binary collision approximation in simulations. The use of marker planes has shown their ability in exploring the evolution of collision cascade anisotropies.

The distributions of the recoil vector fluxes have been studied in order to investigate the anisotropies of collision cascades. Two kinds of calculations were performed. The corrections to the deflection points of the trajectories were taken into account in both types of calculations but when the fluxes were calculated the corrections were included or omitted keeping the asymptotical trajectories correct. The former calculations show the mass flow in the cascade. It is characterized by the recoil vector flux N_r. The latter calculations result in the modified vector flux N_r^m, which is closely related to the angular distribution of sputtered particles. The position of the marker plays an important role in the case of the recoil flux N_r. This is due to the fact that low-energy recoils do not necessarily cross a marker depending on the magnitude of the backup of the recoil. Near atomic planes the N_r distributions are dominated by the ⟨110⟩ peaks. Those markers further away from atomic planes are either practically structureless or dominated by the ⟨110⟩ peaks.

In the case of the modified recoil flux N_r^m the marker position is not critical with the exception of the recoils moving along the surface direction. The difference between the N_r and N_r^m distributions can be noticed clearly. In the cases of the Molière and the mean potentials the N_r^m distributions show four pronounced ⟨110⟩ peaks in the backward direction, and in the forward direction these peaks will emerge as the depth of the marker increases. The focusing chains and the other mechanisms (e.g., defocused and replacement sequences, low-energy channeling) represent about equal contribution to focusing along the ⟨110⟩ directions in the backward direction. In the forward direction the significance of the head-on collisions and focusing sequences in the ⟨110⟩ peaks grows as the depth of the marker increases. The other mechanisms make, however, a major contribution to these peaks. The erosion of the interaction potential changes markedly the modified recoil flux distribution. In the backward direction the truncated mean potential produces an intense ⟨100⟩ peak, and in the forward direction ⟨111⟩ and ⟨100⟩ peaks in addition to the ⟨110⟩ peaks. The collision sequences and low-energy channeling are the principal mechanisms, whereas the contribution of the focusing chains is minor.

In the case of sputtering of a (100) surface, the distribution of sputtered particles shows four ⟨110⟩ spots and one ⟨100⟩ spot. The anisotropy in the angular distribution of sputtered particles is directly related to the anisotropy of the cascade development. The relation may be studied using the vector fluxes.

ACKNOWLEDGMENTS

The authors are deeply indebted to Dr. Marc Hou for numerous fruitful discussions and critical comments on the manuscript.

---

[1] P. Sigmund, Phys. Rev. **184**, 383 (1969).

[2] P. Sigmund, in *Sputtering by Particle Bombardment I*, edited by R. Behrisch (Springer-Verlag, Berlin, 1981), pp. 9–72.

[3] J.B. Sanders and H.E. Roosendaal, Radiat. Effects **24**, 161 (1975).

[4] U. Littmark and P. Sigmund, J. Phys. D **8**, 241 (1975).

[5] H.E. Roosendaal, U. Littmark, and J.B. Sanders, Phys. Rev. B **26**, 5261 (1982).

[6] H.M. Urbassek, Nucl. Instrum. Methods **B4**, 356 (1984).

[7] K.T. Waldeer and H.M. Urbassek, Nucl. Instrum. Methods **B18**, 518 (1987).

[8] R.H. Silsbee, J. Appl. Phys. **28**, 1246 (1957).

[9] R.S. Nelson, M.W. Thomson, and H. Montgomery, Philos. Mag. **7**, 1385 (1962).

[10] T. Okutani, M. Shikata, S. Ichimura, and R. Shimizu, J. Appl. Phys. **51**, 2884 (1980).

[11] H.H. Andersen, B. Stenum, T. Sørensen, and H.J. Whitlow, Nucl. Instrum. Methods **B6**, 459 (1985).

[12] M. Szymonski, W. Huang, and J. Onsgaard, Nucl. Instrum. Methods **B14**, 263 (1986).

[13] H.L. Bay, W. Berres, and E. Hintz, Nucl. Instrum. Methods **194**, 555 (1982).

[14] W. Berres and H.L. Bay, Appl. Phys. A **33**, 235 (1984).

[15] D.E. Harrison, Jr., Radiat. Eff. **70**, 1 (1983).

[16] D.E. Harrison, Jr., Crit. Rev. Solid State Mater. Sci. **14**, Suppl. 1, 1 (1988).

[17] H.H. Andersen, Nucl. Instrum. Methods **B18**, 321 (1987).

[18] M.T. Robinson, in *Sputtering by Particle Bombardment I*, edited by R. Behrisch (Springer-Verlag, Berlin, 1981), pp. 73–144.

[19] J.B. Gibson, A.N. Goland, M. Milgram, and G.H. Vineyard, Phys. Rev. **120**, 1229 (1960).

[20] C. Erginsoy, G.H. Vineyard, and A. Englert, Phys. Rev. A **133**, 595 (1964).

[21] J.R. Beeler, Jr., J. Appl. Phys. **37**, 3000 (1966).

[22] M. Hautala and H.J. Whitlow, Nucl. Instrum. Methods **B6**, 466 (1985).

[23] H.J. Whitlow and M. Hautala, Nucl. Instrum. Methods **B18**, 370 (1987).

[24] M. Hou, Phys. Rev. B **31**, 4178 (1985).

[25] M. Hou, Phys. Rev. A **39**, 2817 (1989).

[26] M.T. Robinson and I.M. Torrens, Phys. Rev. B **9**, 5008 (1974).

[27] M. Hou and W. Eckstein, IPP Report No. IPP 9/65, Max-Planck-Institut für Plasmaphysiks, München, 1988.

[28] J. Likonen and M. Hautala, Appl. Phys. A **45**, 137 (1988).

[29] G.K. Wehner, J. Appl. Phys. **26**, 1056 (1955); Phys. Rev. **102**, 690 (1956).

[30] W. Eckstein and M. Hou, Nucl. Instrum. Methods **B31**, 386 (1988).

[31] J. Likonen and M. Hautala, J. Phys.: Condens. Matter **1**, 4697 (1989).

[32] J. Likonen and M. Hautala (unpublished).

[33] M. Hautala, Phys. Rev. B **30**, 5010 (1984).

[34] J. Lindhard, M. Scharff, and H.E. Schiøtt, Mater. Fys. Medd. Dan. Vid. Selsk. **33**, No. 14 (1963).

[35] M. Bister, M. Hautala, and M. Jäntti, Radiat. Effects **42**, 201 (1979).

[36] W. Eckstein and J.P. Biersack, Appl. Phys. A **34**, 73 (1984).

[37] W.D. Wilson, L.G. Haggmark, and J.P. Biersack, Phys. Rev. B **15**, 2458 (1977).

[38] B.M. Latta and P.J. Scanlon, Phys. Rev. A **10**, 1638 (1974).

[39] P. Sigmund, A. Oliva, and G. Falcone, Nucl. Instrum. Methods **194**, 541 (1982).

[40] K.H. Beckurts and K. Wirtz, in *Neutron Physics* (Springer-Verlag, Berlin, 1964), pp. 81–83.

[41] H. Goldstein, in *Classical Mechanics* (Addison-Wesley, Reading, Mass., 1959), pp. 55–89.
[42] V.I. Shulga, Radiat. Effects **70**, 65 (1983); **82**, 169 (1984); **84**, 1 (1985).
[43] M. Hou and W. Eckstein, Nucl. Instrum. Methods **B13**, 324 (1986).
[44] Y. Yamamura and W. Takeuchi, Nucl. Instrum. Methods **29**, 461 (1987).
[45] A.L. Southern, W.R. Willis, and M.T. Robinson, J. Appl. Phys. **34**, 153 (1963).

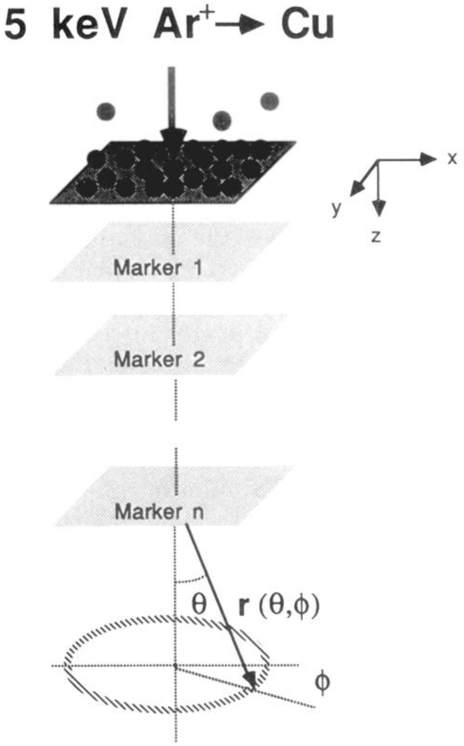

FIG. 2. Schematic illustration of the geometry used in the simulations.